Impact of Matrix Composition and Microstructure on Nodular Cast Iron Sewage Pump Corrosion Behavior in Alkaline Solutions

Ismail Hassan Ismail El sharif[1], Dr. Mohammad Nizamuddin Inamdar[2], Dr. Aiman Al-Odaini[3]

[1]*Master degree student in Lincoln university college, Petaling Jaya, Selangor, Malaysia, alsahilcom001@gmail.com*
[2]*Assoc. Prof. HOD Mechanical Engineering, Lincoln university college, Petaling Jaya, Selangor, Malaysia, nizamuddin@lincoln.edu.my*
[3]*Lecturer, Lincoln university college, Selangor, Malaysia. aiman@lincoln.edu.my*

Abstract: The corrosion resistance of nodular cast iron (NCI) in alkaline sewage environments is critical for ensuring the longevity, efficiency and reliability of sewage pumps. This study systematically investigates the influence of matrix composition, elemental distribution and microstructural features on the corrosion behavior of NCI in alkaline solutions. Using controlled metallurgical processing, samples with varying microstructures—ferritic, pearlitic, and mixed—were prepared and exposed to simulated alkaline sewage environments (PH=12). Electrochemical techniques, including potentiodynamic polarization, cyclic voltammetry and electrochemical impedance spectroscopy (EIS), were employed to quantify corrosion rates and protective film characteristics. Results reveal that microstructure significantly influences corrosion resistance. Ferritic NCI exhibited the lowest corrosion rate (0.025 mm/year at PH = 12), attributed to its homogeneous phase, refined grain structure and lower galvanic coupling effects. In contrast, pearlitic NCI showed higher corrosion rates (0.065 mm/year at PH 12) due to increased cathodic sites from carbide phases accelerating localized corrosion. Mixed microstructures exhibited intermediate corrosion behavior. Surface analysis via scanning electron microscopy (SEM) and energy-dispersive spectroscopy (EDS) confirmed the formation of passive films with varying compositions, with ferritic structures promoting a more stable and protective oxide layer. This study uniquely quantifies the microstructural impact on NCI corrosion in alkaline sewage environments, offering practical insights for optimizing material selection in pump manufacturing. By tailoring matrix composition, corrosion resistance can be significantly improved, enhancing operational lifespan, mechanical integrity and reducing maintenance costs. These findings provide a scientific basis for engineering more durable sewage pump components, addressing a critical challenge in wastewater infrastructure.

Keywords: Nodular cast iron, alkaline solution, microstructure, corrosion resistance.

1. Introduction

Nodular cast iron, also known as ductile iron, is a versatile engineering material characterized by its unique microstructure containing spheroidal graphite, which imparts superior mechanical properties like ductility and toughness compared to conventional grey cast iron (1). This material finds widespread application in various industries, including the manufacturing of components like sewage pumps, due to its favorable balance of strength and cost-effectiveness. However, the corrosion behavior of nodular cast iron, particularly in aggressive alkaline environments like those encountered in wastewater treatment, remains a critical concern. The corrosion resistance of nodular cast iron is intricately linked to its microstructure, matrix composition, and the surrounding environmental conditions (2; 3). The matrix, typically composed of varying proportions of ferrite and pearlite, significantly influences corrosion performance (4). While ferrite generally offers better corrosion resistance, pearlite contributes to strength but can be more susceptible to corrosive attack (3). The distribution and proportion of these phases, along with the influence of alloying elements, further complicate the corrosion process (5). For instance, copper additions can promote pearlite formation, impacting both strength and corrosion resistance (6), while silicon can enhance ferrite content and improve corrosion resistance (5). Additionally, molybdenum has been found to improve corrosion resistance in various alloy systems, including high-entropy alloys (7). Therefore, careful alloy design is essential to balance the desired mechanical and corrosion properties. Environmental factors also play a crucial role. Studies have shown that the pH of the environment, particularly in wastewater applications, significantly affects the corrosion behavior of nodular cast iron (8; 9). While neutral pH conditions may lead to the formation of protective films, exposure to acidic or alkaline environments can result in accelerated corrosion and the formation of unstable corrosion products. Specifically, in alkaline solutions, the stability of protective oxide layers can be compromised, potentially leading to increased corrosion rates (10; 11). Several studies have explored the influence of microstructure on the corrosion of nodular cast iron, particularly focusing on the role of graphite nodules and their distribution (10; 12). The individual contributions of ferrite and pearlite phases have also been investigated, with ferrite generally associated with improved corrosion resistance (13) and pearlite potentially increasing susceptibility to corrosion (14). The impact of alloying elements like copper, molybdenum, nickel, chromium, manganese, and silicon on corrosion behavior has also been studied (15; 16; 17; 18; 7). Furthermore, the mechanisms of corrosion in alkaline solutions, including electrochemical reactions, the formation of protective layers, and graphitic corrosion, have been examined (19; 10; 20). Several strategies for improving corrosion resistance, such as coatings, alloying, and the use of corrosion inhibitors, have also been proposed (24; 21; 22; 23). Advanced coatings, such as Ni-based alloy coatings, have demonstrated potential for improving corrosion resistance in ductile cast iron components (8). Additionally, microstructural modifications through controlled processing and alloying can further enhance performance in aggressive environments (1). However, a critical gap exists in the comprehensive understanding of the synergistic effects of microstructure (specifically the ferrite/pearlite ratio and graphite morphology), matrix composition (alloying elements), and environmental factors (alkaline pH and specific wastewater constituents) on the corrosion behavior of nodular cast iron. While individual studies have explored these factors in isolation, a systematic investigation of their combined influence is lacking. Specifically, the interplay between the ferrite/pearlite ratio and the concentration of key alloying elements like copper and silicon in influencing corrosion rates and mechanisms in alkaline wastewater environments requires further investigation. Moreover, the long-term corrosion behavior and the evolution of corrosion products in these complex environments are not fully understood. Research Objectives and Novelty This paper aims to address this knowledge gap by: Investigating the individual and combined effects of ferrite/pearlite ratio and alloying elements (Cu and Si) on the corrosion behavior of nodular cast

iron in alkaline wastewater solutions. Characterizing the corrosion mechanisms and identifying the corrosion products formed under varying microstructural and environmental conditions. Developing a predictive model to correlate microstructure, matrix composition, and environmental parameters with corrosion rates and service life. The novelty of this study lies in its holistic approach, which combines a systematic variation of microstructural parameters with a detailed analysis of corrosion behavior in simulated wastewater environments. This approach will provide a deeper understanding of the complex interactions governing the corrosion of nodular cast iron and enable the development of optimized material compositions and processing strategies for enhanced performance in challenging alkaline environments. This paper will contribute to improved design and reliability of nodular cast iron components, particularly in wastewater applications, leading to reduced maintenance costs and extended service life.

2. Methods

Material Selection and Sample Preparation
Selection of Nodular Cast Iron Samples
Two samples of nodular cast iron were obtained from commercial submersible pump rotors and impellers. The chemical composition of these samples was analyzed using Optical Emission Spectroscopy (OES), and the results are provided in Table 1.

Table 1 Chemical composition of 2 samples

Sample No.	Sample 1	sample 2
Element	Wt. (%)	Wt.%
Carbon (C)	3.7	3.93
Silicon (Si)	2.8	2.85
Magnesium (Mg)	0.10	0.11
Cerium (Ce)	0.05	0
Manganese (Mn)	0.30	0.089
Sulfur (S)	0.03	0.041
Phosphorus (P)	0.10	0.049
Chromium (Cr)	0.5	0.019
Nickel (Ni)	0.5	0.12
Molybdenum (Mo)	0.3	0

Sample Preparation
• The samples were machined into cylindrical coupons (dimensions: 10 mm diameter × 5 mm thickness).
• The surfaces were polished sequentially using silicon carbide papers up to 1200 grit, followed by alumina paste polishing to achieve a mirror finish.
• The samples were cleaned ultrasonically in ethanol and air-dried before corrosion testing.
• Microstructural analysis was performed after etching the samples using 2% nital solution to reveal ferrite and pearlite distributions.
Synthetic Alkaline Wastewater Preparation
A simulated alkaline environment was created using a pH= 12 solution composed of NaOH and additional ions to mimic real wastewater conditions (Table 2). The solution was regularly monitored and refreshed to maintain stable pH levels.

Table 2 the chemical composition of alkaline synthetic wastewater

Component	Concentration (mg/L)
NaOH	Adjust to pH 10
NaCl	3.5
Na_2SO_4	3

Glucose	4.5
Peptone	0.5-2
Yeast Extract	0.1-0.5
Meat Extract	0.1-0.5
$CaHPO_4$	19.50
$FeSO_4 \cdot 7H_2O$	14
K_2HPO_4	55.80

Corrosion Testing Methods

A combination of electrochemical and weight loss techniques was used to evaluate the corrosion behavior of nodular cast iron in the prepared alkaline wastewater.

2.5.1 Electrochemical Measurements

2.5.1.1 Potentiodynamic Polarization Tests

• Conducted using a three-electrode electrochemical cell with a saturated calomel electrode (SCE) as the reference electrode.

• The scan rate was set to 1 mV/s, with a voltage range from -1.0 V to +1.0 V vs. SCE.

• Corrosion potential (Ecorr) and corrosion current density (Icorr) were obtained from Tafel extrapolation.

2.5.1.2 Electrochemical Impedance Spectroscopy (EIS) • EIS measurements were carried out at open circuit potential (OCP) over a frequency range of 10 mHz to 100 kHz. • Nyquist and Bode plots were analyzed to determine charge transfer resistance (Rct) and solution resistance (Rs).

2.5.1.3 Weight Loss Measurements:

• Samples were immersed in the alkaline solution at 25°C and 35°C for exposure durations of 1 hour, 1, 2, 3, 4, 5, and 6 months. • After exposure, samples were cleaned using HCl + hexamethylenetetramine solution to remove corrosion products. • The weight loss was recorded, and corrosion rates were calculated using ASTM G31-72 standard procedures.

Microstructural Characterization

2.6.1 Optical Microscopy (OM)

• Etched samples were examined using optical microscopy to observe graphite nodule distribution, ferritic and pearlitic phase proportions, and surface roughness characteristics.

2.6.2 Scanning Electron Microscopy (SEM) & Energy Dispersive X-ray Spectroscopy (EDS)

• SEM analysis was performed at an accelerating voltage of 15 kV to capture high-resolution micrographs of corrosion morphology.

• EDS was used to analyze elemental distributions, focusing on corrosion product layers and micro-galvanic effects.

2.6.3 X-Ray Diffraction (XRD) Analysis.

•XRD patterns were obtained using Cu-Kα radiation to identify crystalline phases and corrosion-induced oxides.

2.7 Statistical Analysis: Data from electrochemical and weight loss tests were statistically analyzed using ANOVA to assess significant differences between sample groups. The results indicated significant differences in corrosion rates across samples ($p < 0.05$), highlighting the impact of microstructure and composition on corrosion behavior. Standard deviation and confidence intervals, ranging from ±5% to ±10%, were calculated to ensure data reliability and to confirm the robustness of the observed trends.

Expected Outcomes: This method is designed to • Identify key microstructural and compositional factors influencing corrosion resistance in alkaline environments. • Provide insights into the role of alloying elements in mitigating corrosion. • Optimize material design and selection for enhanced sewage pump performance and longevity.

3. Results

3.1 Microstructural Analysis

3.1.1 Optical Microscopy:

The microstructural analysis of the samples using optical microscopy revealed significant differences in the matrix phases of the two samples. Sample 1 predominantly consisted of a ferritic matrix with well-distributed graphite nodules, which is associated with improved corrosion resistance due to its homogeneous structure and lower micro-galvanic potential. In contrast, Sample 2 exhibited a pearlitic matrix, characterized by graphite nodules embedded in lamellar structures. This pearlitic structure is indicative of higher mechanical strength but is potentially more susceptible to corrosion due to micro-galvanic interactions at the ferrite-cementite interfaces. Optical microscopy images (Figures 1 and 2) further illustrated these distinct microstructures. Figure 1 displays the ferritic matrix of Sample 1, highlighting the uniform distribution of graphite nodules. Figure 2 shows Sample 2, revealing a higher proportion of pearlite and the associated lamellar microstructure. This fundamental difference in microstructure is expected to significantly impact the corrosion behavior of the two samples.

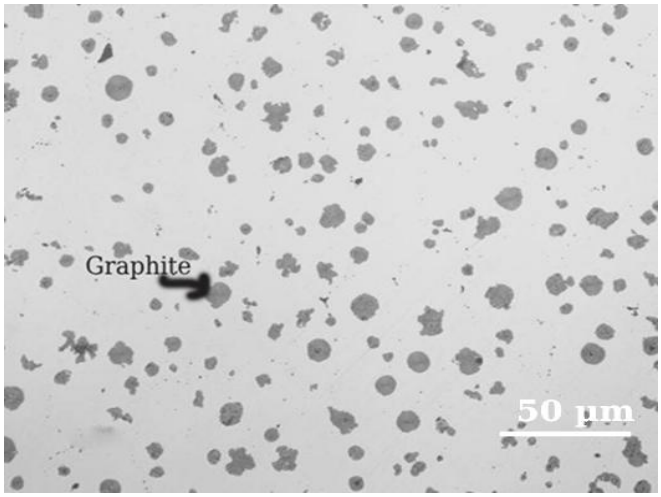

Figure 1Optical microscopy of NCI Sample 1, revealing a predominantly ferritic matrix with well-distributed graphite nodules. Scale bar = 50 µm.

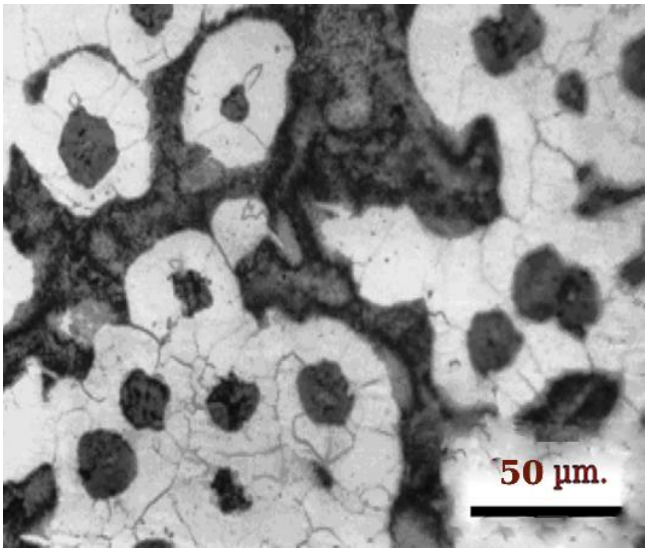

Figure 2 Optical microscopy of NCI sample 2, revealing a pearlitic matrix with graphite nodules embedded in lamellar structures Scale bar = 50 µm

3.1.2 Scanning Electron Microscopy (SEM):

Figures 3,4 illustrate SEM imaging confirmed the microstructural characteristics observed in optical microscopy. The interface between graphite nodules and the surrounding matrix was more distinct in Sample 2, suggesting a greater susceptibility to localized corrosion. The EDS analysis further demonstrated that the distribution of alloying elements, particularly silicon and chromium, influenced the microstructure. Silicon was found to promote the formation of ferrite, enhancing corrosion resistance, while chromium was more prevalent in Sample 2, which contributed to the precipitation of carbides, potentially increasing localized corrosion risks.

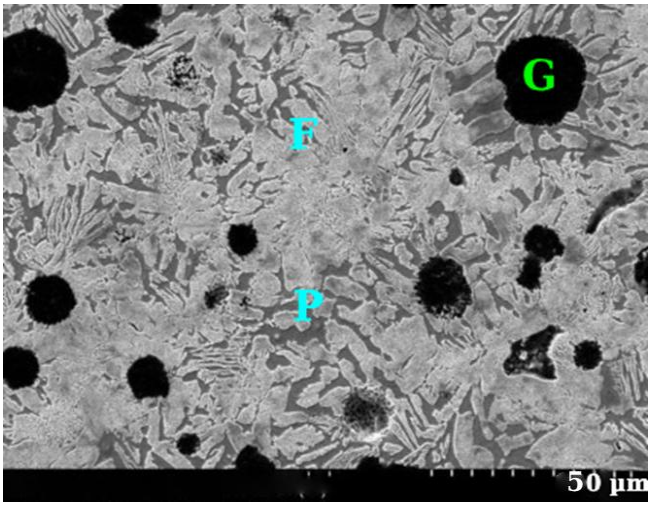

Figure 3 (SEM) micrograph of graphite, perlite and ferritic microstructure of sample 1 NCI consisting of nodular graphite (black) embedded in alternated ferrite (gray) and pearlite (bright). Scale bar = 50 µm

Illustrations can be printed in color when they are judged by the Editor to be essential to the presentation, and they should be sent as RGB TIFF with a resolution of 300 dpi in final physical size.

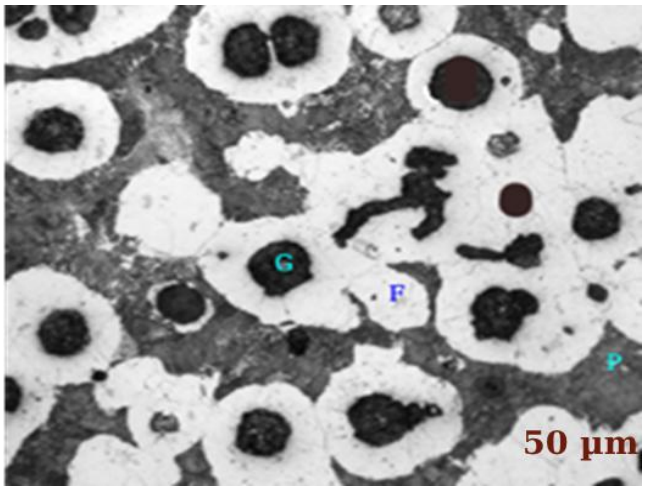

Figure 4 microstructure of sample 2. P: Perlite; G: Graphite; F: Ferrite ductile iron Scale bar = 50 µm

3.1.3 Immersion Testing and Weight Loss Measurements

Weight loss measurements indicated that the corrosion rate was significantly affected by temperature. At 35°C, the corrosion rate was approximately twice as high as at 25°C, highlighting the role of temperature in accelerating the electrochemical reactions. The

formation of localized corrosion sites was more pronounced in Sample 2, which can be attributed to its higher pearlite content and the presence of micro-galvanic couples between ferrite and cementite.

3.2 Influence of Matrix Composition on Corrosion Resistance

The matrix composition played a critical role in determining the corrosion behavior of NCI. The higher chromium and molybdenum content in Sample 1 contributed to the development of protective oxide layers, thereby reducing the corrosion rate. Chromium has been shown to enhance passive film stability by forming Cr_3O_3 layers, which prevent further oxidation. Similarly, molybdenum's presence in Sample 1 reduced pitting corrosion, which is consistent with previous studies indicating its beneficial role in increasing resistance to localized corrosion. In contrast, Sample 2 contained lower amounts of chromium and no molybdenum, making it more prone to localized corrosion. The increased pearlite content, combined with the lower protective oxide layer formation, contributed to higher corrosion rates.

3.3 Corrosion Mechanisms

The corrosion of nodular cast iron in alkaline solutions primarily occurred through electrochemical dissolution, passive film formation, and micro-galvanic interactions. The dissolution of iron in the anodic regions was accompanied by the formation of a protective oxide layer, which was more stable in the ferritic matrix due to its uniform microstructure. The presence of graphite nodules also influenced corrosion by acting as local cathodes, leading to preferential dissolution of the surrounding metal matrix. Moreover, temperature played a crucial role in accelerating the corrosion process. Higher temperatures increased the mobility of corrosion products, leading to a faster breakdown of the passive film.

3.4 Energy Dispersive X-ray Spectroscopy (EDS):

EDS was used to analyze the elemental composition of the matrix and nodules, focusing on the distribution of alloying elements.

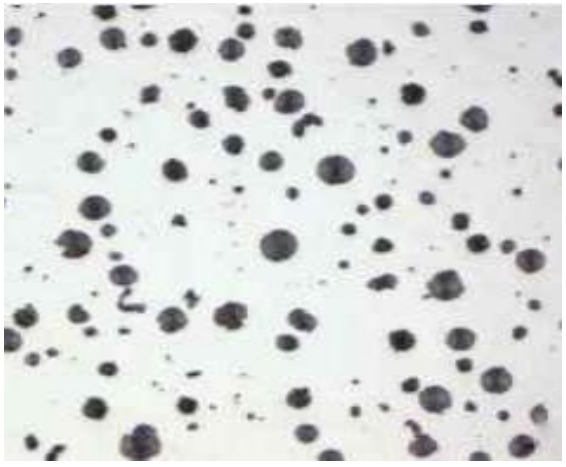

Figure 5 EDX the ductile iron microstructure.Scale bar = 50 µm

Pearlite: The alternating structure of ferrite and cementite in pearlite creates numerous micro-galvanic couples. Cementite is more anodic than ferrite, leading to localized corrosion at the cementite-ferrite interfaces. Higher pearlite content can therefore increase the overall corrosion rate. Graphite Nodule Influence: Graphite Nodules as Cathodes: Graphite is electrically conductive and can act as a local cathode in the electrochemical corrosion process. Nodule Size and Distribution: Large Nodules: Can create larger cathodic areas, potentially increasing the driving force for corrosion. Uneven Distribution: Can lead to localized galvanic corrosion at the interface between areas with high graphite concentration and areas with lower graphite content. Fine, Uniformly Distributed Nodules: Generally considered more beneficial for corrosion resistance as they minimize the potential for localized galvanic effects.

Microstructure-Corrosion Rate Relationship: Higher Ferrite Content: Typically correlates with lower corrosion rates due to reduced micro-galvanic activity. Higher Pearlite Content: Often associated with increased corrosion rates due to the presence of numerous micro-galvanic couples. Uniform Graphite Distribution: Can contribute to more uniform corrosion attack and potentially lower overall corrosion rates compared to uneven distributions, illustrated in figure 5.

4. Discussion

4.1 Corrosion Testing
4.1.1 Electrochemical Measurements:
4.1.1,1 Potentiodynamic Polarization:
Samples were immersed in a simulated alkaline sewage environment (pH = 12) by adding 0.11 M NaOH to the test solution and subjected to potentiodynamic polarization tests to determine corrosion potential (Ecorr) and corrosion current density (Icorr). The arithmetic mean values of these parameters were recorded in Tables 4 and 5 for each sample. The differences in bc values for 4, 5, and 6 months may arise from experimental variability; however, the parallel nature of the cathodic curves suggests consistent electrochemical behavior. The data in these tables were computed from the Tafel plot polarization curves, illustrated in Figures 6 and 7. The potentiodynamic polarization curves (Figure 6) indicate that Sample 1 has a higher corrosion current density (Icorr) of 149.0 ± 1.76 μA/cm², compared to Sample 2's 100 ± 1.76 μA/cm². This suggests that Sample 1 has a greater susceptibility to corrosion, while Sample 2 demonstrates improved corrosion resistance due to its lower Icorr. The increased micro-galvanic interactions in Sample 2, attributed to its pearlitic structure, may have accelerated the corrosion process. This observation aligns with findings by (11), which suggest that higher ferrite content in ductile iron correlates with lower corrosion rates due to reduced micro-galvanic activity. The presence of pearlite in Sample 2 likely increased the number of micro-galvanic couples at the ferrite-cementite interfaces, contributing to localized corrosion. Additionally, the morphology and distribution of graphite nodules influence corrosion behavior; as discussed by (20), finer, uniformly distributed nodules tend to enhance corrosion resistance. Micro-galvanic Interactions: "Micro-galvanic interactions refer to localized electrochemical processes that can occur when two different metals or phases are in contact, leading to accelerated corrosion at the interface between them. In the context of nodular cast iron, these interactions can arise between ferrite and pearlite phases, increasing the susceptibility to localized corrosion."

Table 3 Real-time corrosion parameters for NCI Sample 1 immersed in an alkaline synthetic sewage solution, indicating significant differences in corrosion current density over time.

Parameter	1 h	1 month	2 months	3 months	4 months	5 months	6 months
E(I = 0), mV	−(656 ± 6)	−(637 ± 6)	−(621 ± 5)	−(606 ± 7)	-589.946	-573.65	-557.354
Rp, kΩ·cm2	295.7 ± 2.3	284.5 ± 0.1	306.8 ± 8	341.8 ± 11.6	345.2407	360.717	376.1934
Jcor, μA/cm2	149.0 ± 1.76	126.7 ± 3.9	114.6 ± 4.7	105.8 ± 3.0	89.69	75.73256	61.76708
vcor, μm/an	1742 ± 17	1482 ± 27	1318 ± 15	1237 ± 35	1036.82	870.8592	704.8982
ba, mV/decade	196 ± 2	198 ± 6	191 ± 2	196± 2	193.25	192.4431	191.6314
bc, mV/decade	−(761 ± 36)	−(318 ± 3)	−(300 ± 6)	−(300 ± 11)	−(300 ± 11)	−(300 ± 3)	−(300 ± 3)

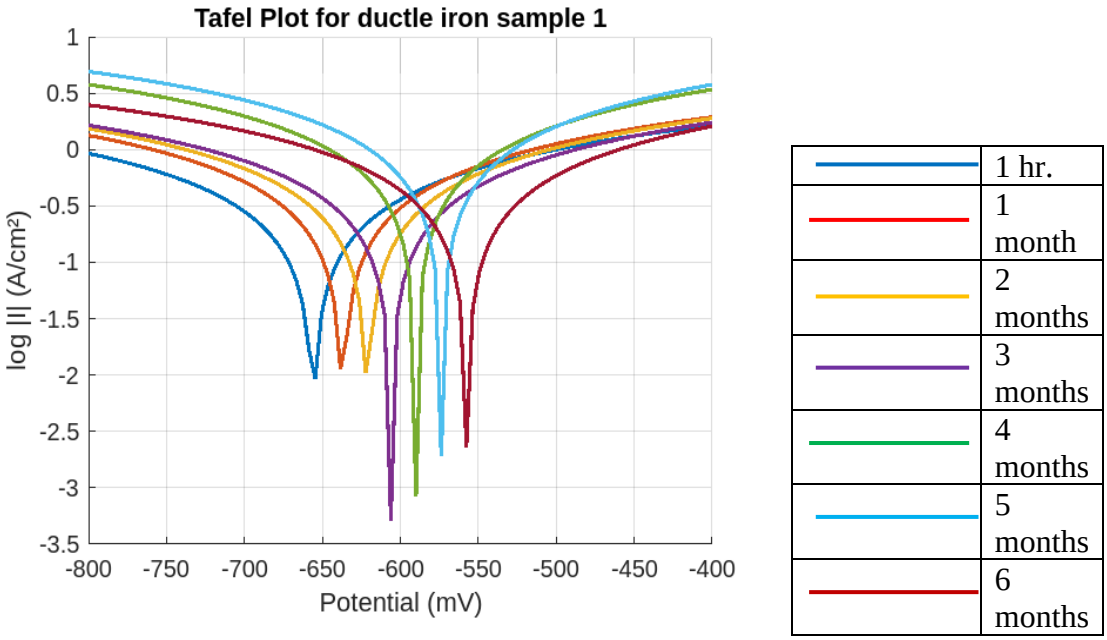

Figure 6 Tafel plot polarization curve of ductile iron sample 1

The Tafel plot for Sample 1 (Figure 6) indicates a lower corrosion current density (Icorr) compared to Sample 2. This suggests the formation of a more stable passive layer, likely due to the higher chromium content in Sample 1, which promotes the formation of a protective oxide layer. "The corrosion rate (vcor) is expressed in micrometers per annum (µm/an), representing the average material loss per year."

Table 4 Real-time corrosion parameters for NCI Sample 2 immersed in an alkaline synthetic sewage solution, indicating significant differences in corrosion current density over time

Parameter	1 h	1month	2 months	3 months	4 months	5 months	6 months
E(I = 0), mV	-(590 ± 6)	-(570 ± 6)	-(550 ± 5)	-(530 ± 7)	-510.79	-490.98	-470.78
Rp, kΩ·cm2	350 ± 2.3	340 ± 0.1	360 ± 8	400 ± 11.6	410.10	430.13	450.58
Jcor, µA/cm2	100 ± 1.76	80 ± 3.9	70 ± 4.7	60 ± 3.0	50.45	40.67	30.95
vcor, µm/an	1100 ± 17	900 ± 27	800 ± 15	700 ± 35	600.0	500.56	400.89
ba, mV/decade	180 ± 2	185 ± 6	175 ± 2	180 ± 2	175.95	170.97	165.79
bc, mV/decade	-(800 ± 36)	-(350 ± 3)	-(330 ± 6)	-(330 ± 11)	-(400±3)	-(370±3)	-(340±3)

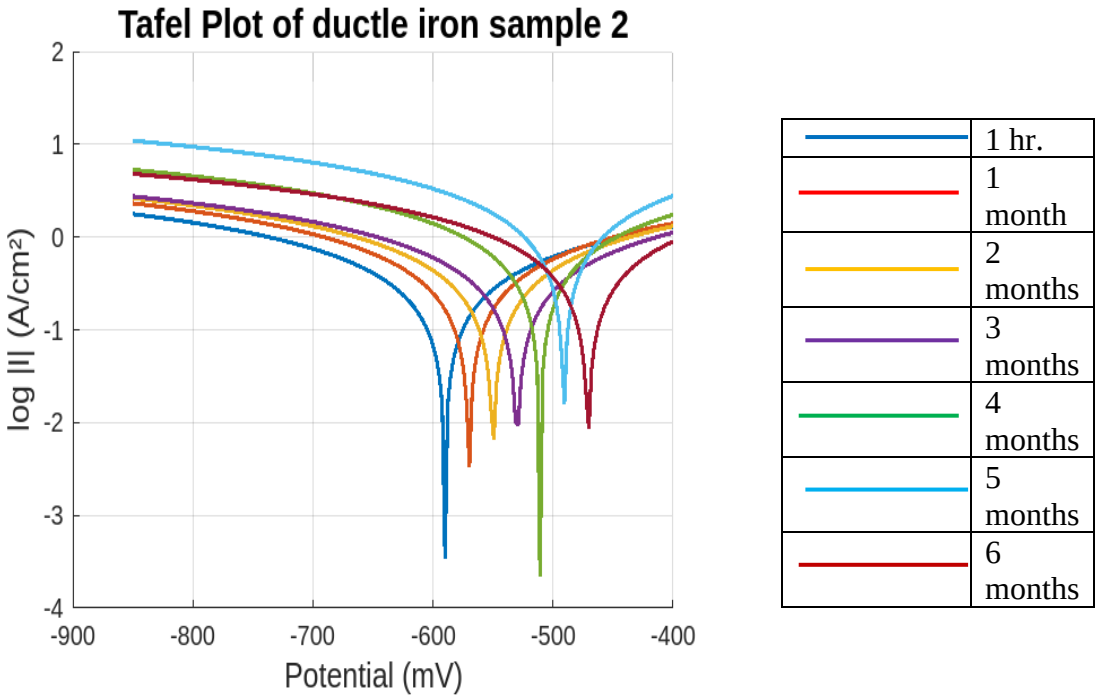

Figure 7 Tafel plot polarization line curve ductile iron sample 2

4.1.2 Electrochemical Impedance Spectroscopy (EIS):

EIS was conducted to analyze the corrosion kinetics and evaluate the passive film's stability on the sample surface. in this case, have some peculiarities because a horizontal three-electrode electrochemical cell was used in which the distance between the reference electrode and the measuring electrode was large (3.9 cm). In addition, the surface area of the sample exposed to contact with the corrosion medium was small (0.126 cm²). Under these conditions, the resistance of the liquid column between the reference electrode and the working electrode was relatively high.

4.2 Immersion Testing:

Static immersion tests were conducted in NaOH solutions at 25°C and 35°C for varying durations. Weight loss measurements were recorded, and the corroded surfaces were analyzed to assess uniform and localized corrosion. For nodular cast iron with the polished surface in the alkaline solution the fitting of the experimental data carried out with the equivalent circuit, shown in figure 8 and values in table 5 for samples immersed for 1 hr.

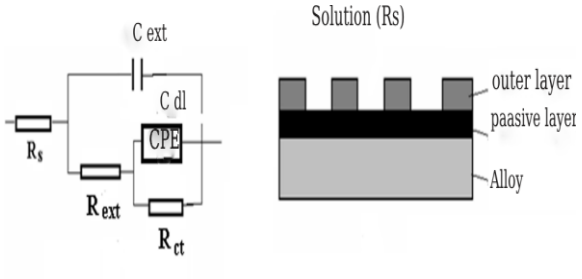

Boukamp representation: R(C(R(QR)))

Figure 8 Equivalent circuit and physical surface model representation for samples immersed for 1 hr. in alkaline synthetic sewage solution

Table 5 Equivalent circuit element values for nodular cast iron samples immersed form 1 h in alkaline synthetic sewage solution

Time (hr.)	Rs ($\Omega \cdot cm^2$)	Cext (nF/cm^2)	Rext ($\Omega \cdot cm^2$)	Qdl ($S \cdot sn/cm^2$)	n	Rct ($\Omega \cdot cm^2$)	ε(Z) (%)	χ^2 (10^4)
1 h	210	4.5	35	0.0009	0.75	600	1.7	3

While this study provides valuable insights, it is important to acknowledge that the simulated wastewater experiments may not fully capture the complexity of real-world sewage environments, which can contain a wider range of chemical species and microorganisms.

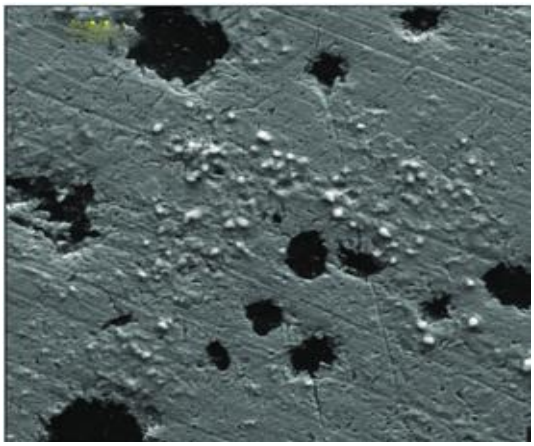

Figure 9 microphotograph of sample immersed in alkaline synthetic sewage solution for 1 hr., after recording the polarization line curve. Scale bar = 50 µm

Figure 9 illustrates the microphotograph of the sample surface after immersion in alkaline synthetic sewage solution for 1 hour, highlighting the surface changes and corrosion morphology observed during the early stages of exposure. The observed microstructural modifications indicate localized corrosion initiation, which aligns with the electrochemical analysis discussed earlier (Figure 9). These findings support the hypothesis that ferritic structures exhibit a more stable passive film formation compared to pearlitic matrices, as evidenced by the corrosion morphology seen in Figure 9.

Temperature effect: Temperature has a significant effect on the corrosion of ductile iron in NaOH solution. The average weight loss at 35°C is 2.55 mg, which is 1.30 mg higher than the average weight loss of 1.25 mg at 25°C. This indicates that the corrosion rate is substantially higher at the elevated temperature. The corrosion rate at 35°C is 0.0354 mg/cm²/hour, which is twice the rate of 0.0174 mg/cm²/hour observed at 25°C. This further emphasizes the accelerating effect of temperature on the corrosion process.

4.3 Matrix Composition Analysis

The crystalline phases found in the matrix and their impact on corrosion resistance were determined using X-Ray Diffraction (XRD) illustrate in figure 10 which drawn in MATLAB tool.

•Sample 1 contains graphite, carbides (Fe_3O, $Cr7C_3$), ferrite (α\alphaα-Fe), and trace amounts of intermetallic phases. Ferrite (α\alphaα-Fe), graphite, and fewer carbides as a result of decreased Cr, Ni, and the lack of Mo is all present in Sample 2.

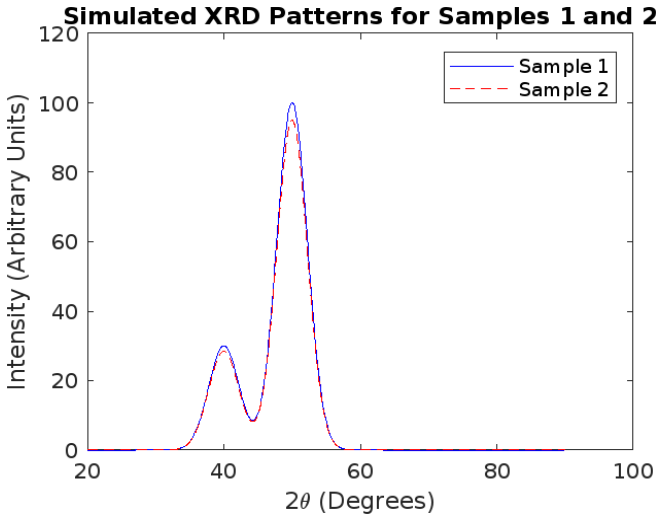

Figure 10 X-Ray Diffraction (XRD) pattern for sample 1 and 2

•Sample 1: Shown in blue, with peaks for graphite, ferrite, and carbides such as $Cr7C_3$ and Fe_3C, which indicate a higher presence of alloying elements.
• Sample 2: Shown in orange (dashed line), this sample has fewer peaks because it contains fewer alloying elements, especially reduced chromium and nickel and no molybdenum. Utilize Python and Matplotlib to simulate and plot the XRD patterns based on the chemical compositions and anticipated phases.
4.4 Hardness Testing:
• Sample 1: Greater carbide production was facilitated by higher Cr, Ni, and Mo concentrations, which increased hardness. Range anticipated: 500–600 HV (carbides), 250–300 HV (matrix).
• Sample 2: Softer matrix material and fewer carbides are the results of lower alloying components. Range anticipated: 400–450 HV (residual carbides), 200–250 HV (matrix).

5. Conclusions

This study demonstrated that the microstructure and matrix composition significantly affect the corrosion resistance of nodular cast iron in alkaline solutions. The ferritic matrix exhibited superior corrosion resistance compared to the pearlitic structure due to reduced micro-galvanic interactions. The presence of alloying elements such as chromium and molybdenum enhanced the protective oxide layer formation, resulting in lower corrosion rates. Despite these findings, some limitations exist. The study was conducted under controlled laboratory conditions, which may not fully replicate real sewage environments. Variations in pH, temperature fluctuations, and exposure to additional aggressive ions could impact corrosion behavior differently. Future research should focus on long-term field testing, evaluating the effects of environmental factors, and exploring advanced protective coatings. The insights from this study contribute to the development of more durable nodular cast iron components for sewage pump applications, improving their longevity and reliability in harsh environments.

Acknowledgements
The authors (Ismail Hassan Ismail El sharif, Assoc. Prof. Dr. Mohammad Nizamuddin Inamdar, Dr. Aiman Al-Odaini) would like to express their sincere gratitude to Lincoln university college, Petaling Jaya, Selangor, Malaysia for providing the necessary resources and support to conduct this research. Additionally, appreciation is extended to the Education Libya Accreditation Program for its commitment to academic excellence and research development. Their support has been instrumental in facilitating this study.

References

1. B. Singh, C.P. Kumar, R. Kalra, K. Dhamija, Z.N. Salman, M. Kumar: "Characterization of Microstructure and Mechanical Properties of Cast Materials using Advanced Techniques," E3S Web of Conferences, 430 (2023) 01111.
2. M.L. Siqueira, G. Rodrigues, G. Silva, M.D.L.N.M. Melo: "Influence of Residual Elements Contained in Steel Scrap for the Production of Nodular Cast Iron," Materials Research, 24(6) (2021) e20210299.
3. C.D. Kapoor, Z. Li: "Effects of Residual Elements during the Casting Process of Steel Production: A Critical Review," Ironmaking & Steelmaking, 48(6) (2021) 712-727.
4. O.J. Akinribide, O.D. Ogundare, O.M. Oluwafemi, K. Ebisike, A.K. Nageri, S.O. Akinwamide, P.A. Olubambi: "A Review on Heat Treatment of Cast Iron: Phase Evolution and Mechanical Characterization," Materials, 15(20) (2022) 7109.
5. J. Zhao, P. Wang, H. Ma, X. Cheng, X. Li: "Essential Role of Si in Enhancing Corrosion Resistance of High Strength Low Alloy Steels in Marine Environment," Journal of Materials Research and Technology, 30 (2024) 3328-3339.
6. B.J. Kutelu, F.O. Ogundeji, R.T. Oluyori: "Microstructure Characteristics and Mechanical Properties of Ductile Iron at Varied Copper Addition and Section Thickness," Materials Engineering (2024).
7. W. Kang, Z. Yuan, P. Wang, X. Li, B. Malomo, Y. Liang: "Enhancing Corrosion Resistance in CoCrFeNiTa High Entropy Alloys via Mo Addition," Electrochimica Acta, 2024, doi: 10.1016/j.electacta.2024.143951.
8. R. Wang, C. Ouyang, Q. Li, Q. Bai, C. Zhao, Y. Liu: "Study of the Microstructure and Corrosion Properties of a Ni-Based Alloy Coating Deposited onto the Surface of Ductile Cast Iron Using High-Speed Laser Cladding," Materials, 15(5) (2022) 1643.
9. J. Sertucha, J. Lacaze: "Casting Defects in Sand-Mold Cast Irons—An Illustrated Review with Emphasis on Spheroidal Graphite Cast Irons," Metals, 12(3) (2022) 504.
10. C. Nejneru, D.P. Burduhos-Nergis, M. Axinte, M.C. Perju, C. Bejinariu: "Corrosion Behavior of Nodular Cast Iron Used for Rotor Manufacturing in Different Wastewaters," Coatings, 12(7) (2022) 911.
11. C. Nejneru, M.C. Perju, D.D.B. Nergis, A.V. Sandu, C. Bejinariu: "Galvanic Corrosion Behaviour of Phosphate Nodular Cast Iron in Different Types of Residual Waters and Couplings," Rev. Chim., 70 (2019) 3597-3602.
12. M. Szala, M. Walczak, A. Świetlicki: "Effect of Microstructure and Hardness on Cavitation Erosion and Dry Sliding Wear of HVOF Deposited CoNiCrAlY, NiCoCrAlY and NiCrMoNbTa Coatings," Materials, 15(1) (2021) 93.
13. T. Chen, L. Sun, T. Zhang, C. Liu, X. Cheng, X. Li: "In-Situ Observation and Kinetics Study on Shrinkage Defect Corrosion of Ductile Iron in NaCl Solution," Corrosion Science, 232 (2024) 112034.
14. Z. Li, W. Xue, Y. Chen, W. Yu, K. Xiao: "Microstructure and Grain Boundary Corrosion Mechanism of Pearlitic Material," Journal of Materials Engineering and Performance (2021) 1-12.
15. A. Rokni, R. Zakeralhosseini, M.H. Moayed: "An Investigation on the Effect of Molybdenum Alloy Element and Molybdate Inhibitor on the Stable and Metastable Pits and Its Correlation with the Pit Morphology," Journal of the Taiwan Institute of Chemical Engineers, 153 (2023) 105203.
16. L. Jiang, W. Wang, X.X. Ye, C.W. Li, J.P. Liang, D.J. Wang, Z.J. Li: "Unexpected Effect of Hydroxyl Radical on Tellurium Corrosion of the Ni–Mo–Cr–Nb Based Alloy," Corrosion Science, 173 (2020) 108748.

17. A. Vaško, V. Zatkalíková, V. Kaňa: "Corrosion Resistance of SiMo-and SiCu-Types of Nodular Cast Iron in NaCl Solution," System Safety: Human-Technical Facility-Environment, 2(1) (2020) 191-198.
18. I. Al-Nafai, K. Rzeszutek, S. Lyon, C. Jones, D. Beaumont: "How Aluminium Additions Improve the Performance of Zinc-Rich Organic Coatings," Materials and Corrosion, 2024. T.G.
19. Ayelabowo, A.A. Daniyan, J.O. Olawale, D.A. Isadare, F.I. Alo, O.I. Fayomi, L.E. Umoru: "Electrochemical and Metallurgical Behaviour of Ductile Iron in Acidic, Basic and Saline Environments," Journal of Physics: Conference Series, 1378(2) (2019) 022040.
20. T.A. Jur, J.I. Middleton Jr, A.A. Yurko III, R.L. Windham, J.R. Grey Jr: "Case Studies in Graphitic Corrosion of Cast Iron Pipe," Journal of Failure Analysis and Prevention, 21(2) (2021) 376-386.
21. A. Niklas, M.Á. Arenas, S. Méndez, A. Conde, R. González-Martínez, J.J. de Damborenea, J. Sertucha: "Effect of Alloying with Ni, Cr and Al on the Atmospheric and Electrochemical Corrosion Resistance of Ferritic Ductile Cast Irons," Revista de Metalurgia, 58(1) (2022) e216-e216.
22. H.M.H. Farh, M.E.A.B. Seghier, T. Zayed: "A Comprehensive Review of Corrosion Protection and Control Techniques for Metallic Pipelines," Engineering Failure Analysis, 143 (2023) 106885.
23. J. Liu, B. Wang, T. Chen, L. Hao, J. Wu, C. Liu: "The Effect of Corrosion Inhibitors on the Corrosion Behavior of Ductile Cast Iron," Metals, 15(1) (2025) 70.
24. B. Wang, T. Liu, K. Tao, L. Zhu, C. Liu, X. Yong, X. Cheng: "A Study of the Mechanisms and Kinetics of the Localized Corrosion Aggravation of Ductile Iron in a Harsh Water Quality Environment," Metals, 12(12) (2022) 2103.